



Characterization of the microstructure, microsegregation, and phase composition of ex-situ Fe–Ni–Cr–Al–Mo–TiC_p composites fabricated by three-dimensional plasma metal deposition on 10CrMo9–10 steel

Łukasz Rakoczy¹ · Kevin Hofer² · Małgorzata Grudzień-Rakoczy³ · Bogdan Rutkowski¹ · Marcin Goły¹ · Torsten Auerbach² · Rafał Cygan⁴ · Kevin Gordon Abstoss⁵ · Anna Zielińska-Lipiec¹ · Peter Mayr⁶

Received: 4 April 2020 / Revised: 18 September 2020 / Accepted: 26 September 2020

© The Author(s) 2020

Abstract

Quaternary powder mixtures $y\text{Ni}-20\text{Cr}-1.5\text{Al}-x\text{TiC}_p$ ($y = 78.5, 73.5, 68.5$; $x = 0, 5, 10$) were deposited on ferritic 10CrMo9–10 steel to form on plates ex-situ composite coatings with austenitic-based matrix. Plasma deposition was carried out with various parameters to obtain eight variants. The microstructure, chemical composition, phase constitution, phase transformation temperatures, and microhardness of the two reference TiC_p-free coatings and six ex-situ composites were investigated by X-ray diffraction, scanning and transmission electron microscopy, energy-dispersive X-ray spectroscopy, thermodynamic simulation, and Vickers microhardness measurements. All composites had an austenite matrix with lattice parameter $a = 3.5891-3.6062 \text{ \AA}$, calculated according to the Nelson–Riley extrapolation. Microstructural observations revealed irregular distribution of TiC_p in the composites. Large particles generally occurred near the external surface due to the acting buoyancy effect, whereas in the interior smaller particles, with an equivalent radius around 0.2–0.6 μm , were present. Due to initial differences in the chemical composition of powder mixtures and also subsequent intensive mixing with the low-alloy steel in the liquid pool, the matrix of the composites was characterized by various chemical compositions with a dominating iron concentration. Interaction of TiC_p with matrix during deposition led to the formation of nano-precipitates of M₂₃C₆ carbides at the interfaces. Based on the ThermoCalc simulation, the highest solidus and liquidus temperatures of the matrix were calculated to be for the composite fabricated by deposition of 73.5Ni–20Cr–1.5Al–5TiC_p powder mixture at $I = 130 \text{ A}$. The mean microhardness of the TiC_p-free coatings was in the range 138–146 $\mu\text{HV}0.1$, whereas composites had hardnesses at least 50% higher, depending on the initial content of TiC_p.

Keywords MMC · Composite · Secondary phases · 3DPMD · Ex situ

1 Introduction

For several years, a dynamic development has been observed for manufacturing techniques of metal matrix composites (MMCs), which produce many materials for the automotive, power, and aerospace industries [1, 2]. They attract special attention due to the relatively low cost and high-performance fabrication, which caused a shift in the research direction from monolithic to composite materials [3, 4]. Manufacturing techniques can be classified on the basis of the metallic matrix temperature processing into two categories, namely liquid state and solid-state processes. The main aim of MMCs' preparation is to keep the physical and chemical properties both of the matrix and particles, which makes it possible to create a combination of properties that cannot be achieved separately [5, 6]. These composites combine the

✉ Łukasz Rakoczy
lrakoczy@agh.edu.pl

¹ Faculty of Metals Engineering and Industrial Computer Science, AGH University of Science and Technology, Mickiewicza 30, 30-059 Kraków, Poland

² Chair of Welding Engineering, Chemnitz University of Technology, 09126 Chemnitz, Germany

³ Łukasiewicz Research Network, Kraków Institute of Technology, Zakopiańska 73, 30-418 Kraków, Poland

⁴ Investment Casting Division, Consolidated Precision Products, Hetmańska 120, 35-078 Rzeszów, Poland

⁵ CEWUS Chemnitzer Werkstoff- Und Oberflächentechnik GmbH, Neefestraße 80a, 09119 Chemnitz, Germany

⁶ Department of Mechanical Engineering, Technical University of Munich, Arcisstraße 21, 80333 Munich, Germany

strength and rigidity of reinforcing non-metallic particles with a ductile metal matrix. Frequently also, they have a lower density which reduces the weight of the final components [7].

For high-temperature applications, nickel-base alloys and austenitic stainless steels are preferred as the matrices for refractory composites, because they have high strength and ductility at elevated temperatures, as well as good hot corrosion and oxidation resistance [8, 9]. For face-centered cubic (FCC) crystal structure, the rates of the thermally activated processes are relatively low [10]. The reinforcement particles are selected taking into account their reactivity with the metal matrix, wetting capability, coefficient of thermal expansion, and density [11]. Ceramic particles, having significantly higher Young's moduli than that of the matrix, enable the composite to bear the maximum stress without cracks [12]. Fractured particles are not only less effective in accommodation of stresses, but also, depending on their morphology, can lead to the formation of discontinuities, being detrimental to Young's modulus and strength [13]. The selected strengthening particles should be characterized by a small difference in thermal expansion coefficient in comparison to the matrix to generate the compressive or tensile stresses during service. These stresses on the interfaces can increase the density of dislocation networks acting as an additional strengthening factor, especially favorable in systems with smaller particles [14]. Mortensen [15] postulated that too high a difference in those coefficients leads to microcrack formation. The group of particles strengthening the metal matrix includes oxides, carbides, intermetallics, nitrides, borides, and silicides. They are introduced into the matrix in the form of nearly spherical particles with various sizes, irregular blocks, whiskers, and long fibers [16–19]. Arsenault [20] indicated that, in contrast to equiaxed particles, discontinuous reinforcements with an aspect ratio higher than 1 (platelets and whiskers) give a stronger contribution to raising the dislocation density during deformation. The presence of sharp edges may promote premature formation of cracks and significantly shorten the service time. Volume fraction of particles varies in a wide range from a few to several dozen, depending on the required mechanical properties, but increasing the volume fraction of particles is not without consequences [21]. After crossing a certain value, not only the ductility decreases rapidly, but often also mechanical strength, especially at high temperatures [22]. To overcome this limitation, a metal matrix should be characterized by superior heat resistance and also be highly compatible with the reinforcement [23]. If the metal matrix of the composite is a precipitation hardening alloy, during the production of a composite upon solidification and cooling of the alloy matrix, microstructural changes may include chemical reactions of the particles with the alloy matrix and formation of precipitates [24, 25]. Particularly important are

matrix/particle interfaces and their vicinities. The bonds at the interface have a significant impact on the final properties. It is widely recognized that relatively weak interface bonds increase the susceptibility to cracking [26]. Additionally, partial dissolution of precipitates leads to enrichment of the matrix in alloying elements, causing formation of secondary phases. In composite Inconel 625/TiB₂, a transition layer enriched in Ti and Mo around TiB₂ particles was observed by Zhang [27]. A promising phase to strengthen the FCC matrix is TiC with regular NaCl structure B1-type (Strukturbericht notation), with the melting 3065 °C, low density (4.93 g/cm³), and high Young's modulus at intermediate temperatures (350 GPa at 700 °C) [28, 29]. Titanium carbide is also one of the hardest refractory metal carbides with a Vickers hardness of 19.6–31.4 GPa and can be expected to improve the abrasion resistance of many different metal matrices. The wetting angle is 30°, which indicates good binding with a pure Ni-matrix [30].

Metal matrix composites, due to their unique combination of high mechanical properties, wear, oxidation, and corrosion resistance, are a promising group of materials for layers to protect steel surfaces in harsh conditions. Nevertheless, work focused on the fabrication and subsequent characterization of MMCs deposited on low-alloy steels is still missing. Three-dimensional plasma metal deposition (3DPMD), due to its high working flexibility and high designability, can be successfully applied to fabricate particle-reinforced ex-situ composites. The main aim of this work was to characterize the microstructure, microsegregation, phase composition, and microhardness of Fe–Ni–Cr–Al–Mo–TiC_p ex-situ composites deposited on ferritic 10CrMo9–10 steel by 3DPMD.

2 Experimental procedure

2.1 Fabrication of Fe–Ni–Cr–Al–Mo–TiC_p composites by three-dimensional plasma metal deposition

Ni, Cr, Al, and TiC powders (Fig. 1) were used to produce Ni–Cr–Al–TiC_p mixtures. Nickel particles had a spherical morphology with a diameter around 178 μm (± 22 μm). Chromium had a platelet morphology of varying sizes from several micrometers to large particles exceeding 100 μm. Aluminum and TiC_p powders had similar morphology of geometric blocks, but they showed differences in surface roughness. TiC powder morphology was conglomerate-like, and so was not divided into fractions to obtain a composite with irregular distribution of particles, with the largest near the surface and fine in the interior. For the deposition, three mixtures presented in Fig. 2 were prepared: (wt%): (1) 78.5Ni–20Cr–1.5Al–0TiC_p;

Fig. 1 Microstructure of raw powders: **a** Ni; **b** Cr; **c** Al; **d** TiC_p

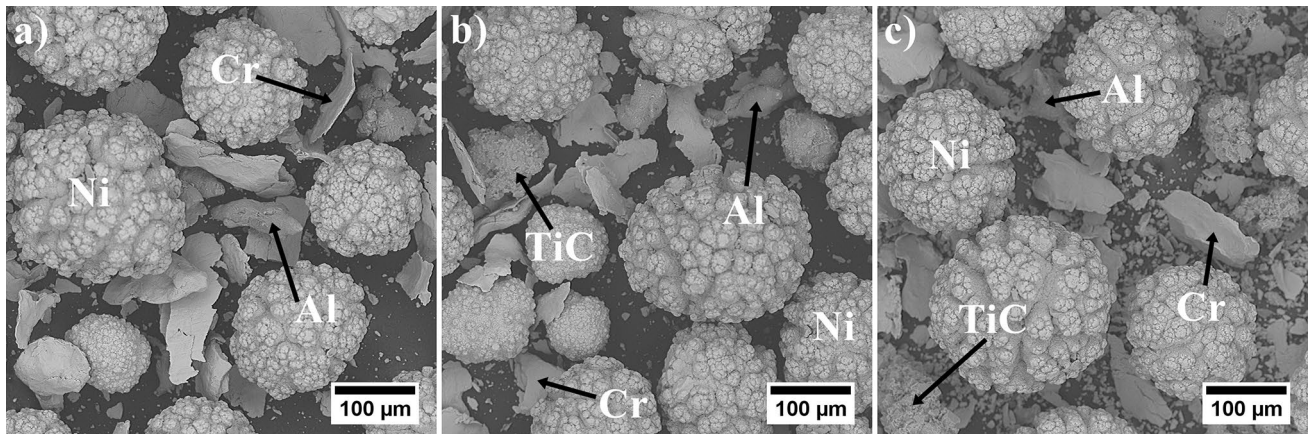
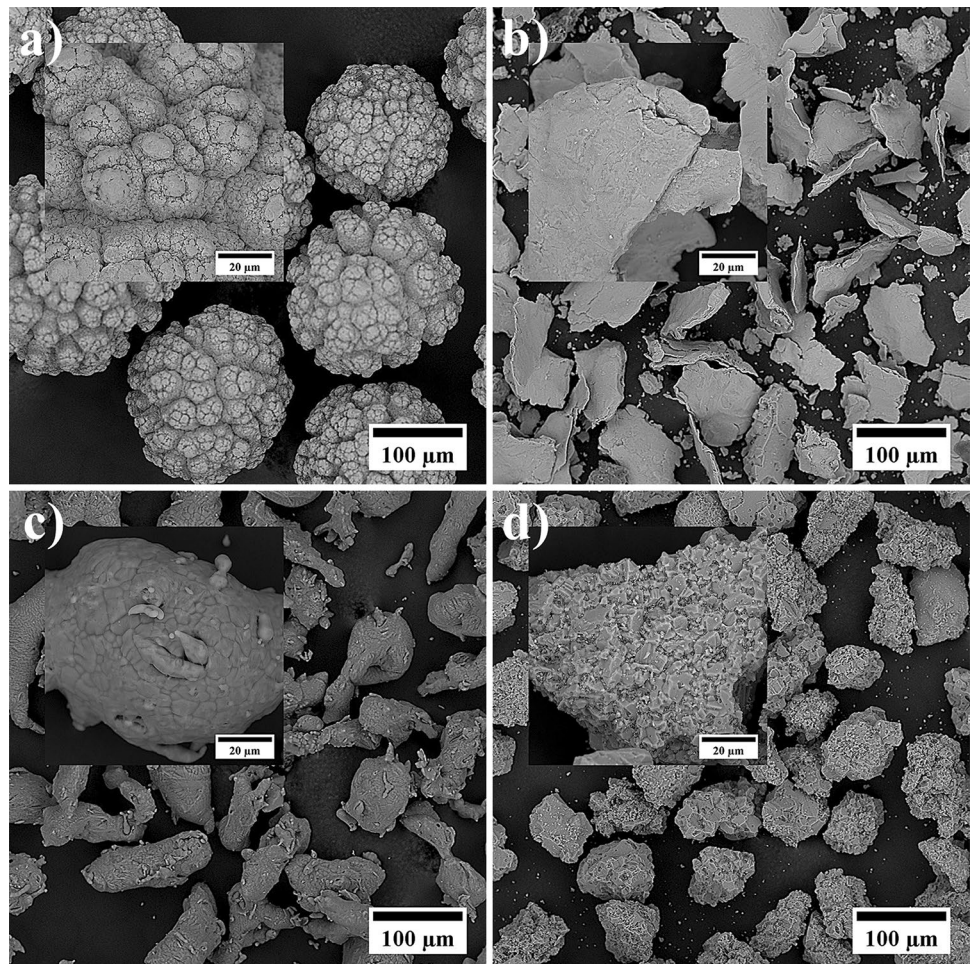


Fig. 2 Microstructure of mixed powders: **a** 0% TiC_p ; **b** 5% TiC_p ; **c** 10% TiC_p

(2) $73.5Ni-20Cr-1.5Al-5TiC_p$; (3) $68.5Ni-20Cr-1.5Al-10TiC_p$, and subsequently, these were subjected to homogeneous mixing for 1 h in a three-dimensional Turbula® mixer.

Single layers 80 mm in length and 20 mm in width were produced (Fig. 3a) on 10CrMo9–10 steel support plates ($150 \times 60 \times 8$ mm). The chemical composition of the steel, determined by optical emission spectroscopy (OES), was (wt%): Cr: 2.1, Mo: 0.92, Mn: 0.56, Si: 0.25, Cu: 0.02, C:

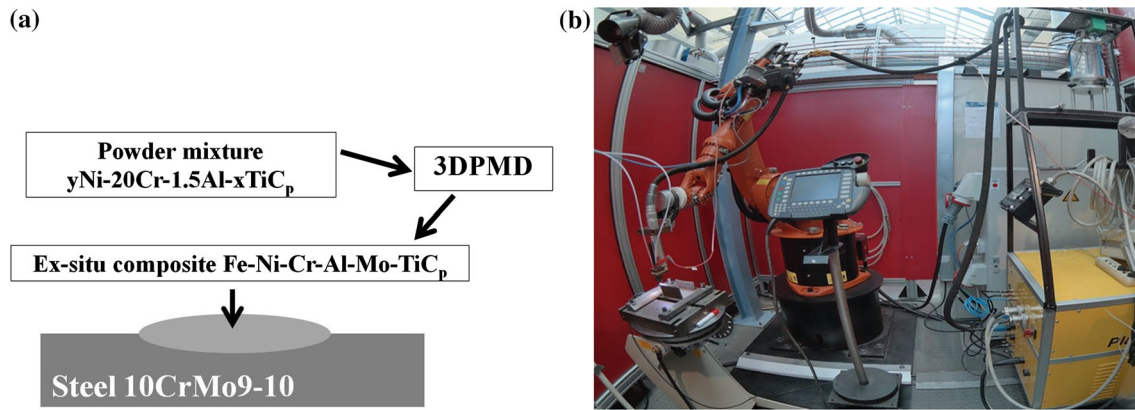


Fig. 3 a Scheme of the deposition process; b experimental setup of three-dimensional plasma metal deposition

0.09, P: 0.012, Ni: 0.04, S: 0.003, Fe: Bal. This grade of steel was chosen due to wide application for components in the power industry and the constant need to increase their corrosion and wear resistance properties. Base plates for the process were preheated to 100 °C. The experimental setup of three-dimensional plasma metal deposition is presented in Fig. 3b. Power source was PlasmaStar 500 ($I_{\max} = 500$ A) in combination with the welding torch MV230 ($I_{\max} = 230$ A). A Plasmastar PF II disk conveyor with a feed rate up to 250 g/min. was used for powder supply. A six-axis articulated arm robot Kuka KR6-2 was used as the manipulation system. The electrode-type WC20 (Ce-1.47–1.79%, CeO₂-1.80–2.20%) with a diameter 4 mm and angle grinding 30° was used. The distance between the plasma anode and the workpiece was 10 mm and the electrode set back was 1.5 mm. During a composite fabrication, the rate of shielding gas was 12 l/min, carrier gas 3 l/min, and plasma gas 1.5 l/min. In all cases, argon 4.6 was used. The selection of parameters (Table 1) took into account the stir of $y\text{Ni}-20\text{Cr}-1.5\text{Al}-x\text{TiC}_p$ ($x = 0, 5, \text{ or } 10$; $y = 78.5, 73.5$ or 68.5) mixtures with the low-alloy steel characterized by body-centered cubic structure (BCC) to obtain the

$\text{Fe}-\text{Ni}-\text{Cr}-\text{Al}-\text{Mo}-\text{TiC}_p$ ex-situ composites with austenitic Fe-based matrix.

2.2 Specimen preparation

Microstructure observations and analyses were performed using the following techniques: X-ray diffraction (XRD), light microscopy, scanning electron microscopy, energy-dispersive X-ray spectroscopy, transmission electron microscopy (TEM), high-resolution transmission electron microscopy (HRTEM), thermodynamic simulations, and Vickers microhardness measurements. X-ray diffraction experiments were carried out on a Bruker D8 Advance diffractometer, using Co K_α radiation ($\lambda = 1.79$ Å) in Bragg–Brentano geometry. The samples (polished on the composite face) were measured at an interval of 2θ between 40° and 130° with step size 0.04°. The texture of the matrix was determined as the relative intensity of selected diffraction peaks. Precise calculation of the matrix lattice parameters was based on the measurements from XRD using Nelson–Riley [31] extrapolation function $(\cos^2\theta/\sin\theta) + (\cos^2\theta/\theta)$. Metallographic samples were wet cut from the prepared specimens, ground with SiC sandpaper and then polished on a diamond

Table 1 Parameter of 3DPMD process

No	Current (A)	Deposition rate (cm/min)	Powder feed rate (g/min)	Composition of powder mixture (wt%)	Thickness of the layer (mm)
1	130	30	22	78.5Ni–20Cr–1.5Al–0TiC _p	1.0 (±0.1)
2	160	60	32		1.8 (±0.2)
3	100	30	15	73.5Ni–20Cr–1.5Al–5TiC _p	3.7 (±1.2)
4	130				2.8 (±0.6)
5	160	60			2.3 (±0.6)
6	100	30	15	68.5Ni–20Cr–1.5Al–10TiC _p	4.4 (±0.4)
7	130				3.7 (±0.4)
8	160	60			3.1 (±0.5)

suspension (6 μm , 3 μm , 1 μm , 0.25 μm). Microstructure images were recorded for unetched samples by light- (LM) and scanning electron (SEM) microscopy. To calculate the volume fraction and stereological parameters of fine TiC_p in the microstructure, images were subjected to binarization and analysis by ImageJ commercial software. The regions of TiC_p were determined, and then, their size was presented as the equivalent radius. To compare the morphology of fine precipitates, non-dimensional TiC_p shape factor expressed as $\zeta = 4\pi A/P^2$ (A —area, P —perimeter) was calculated. The measurements were conducted in ten locations in two rows, above (500 μm and 1000 μm) and below (500 μm and 1000 μm) horizontal line of the steel plate, separately. Distance between single measurements in one row was also 500 μm . The concentration of alloying elements in Fe–Ni–Cr–Al–Mo– TiC_p composites was determined by SEM–EDX and based on measurements in 10 different locations. One measurement covered the area 2500 μm^2 (50 \times 50 μm). The analyses of composites chemical composition were carried out in above the horizontal line of the steel plate (area which is potentially exposed to external service environment). The procedure was similar to particle's analysis, with the space between the rows and single measurements being 1 mm, instead of 500 μm . The linear distribution of elements in the area of the fusion line was carried out for 134 μm length. Samples for interface TiC_p/γ analysis by transmission electron microscopy were first ground mechanically to about 0.05 mm, and then 3 mm disks were punched and dimpled on each side. The last stage was thinning by Ar^+ ion beam (PIPS of Gatan) with low angles. The probe Cs-corrected FEI Titan³ G2 60–300 with ChemiSTEM system (Thermo Fisher Scientific) was utilized to obtain nanostructure of the composite and chemical composition mapping in the area of secondary phases. The Fast

Fourier Transformation (FFT) on high-resolution images were performed to reveal the position of diffraction peaks. The sample no. 7 was chosen as a representative variant. The selected area electron diffractions and FFT images were analyzed with the JEMS software. The thermodynamic simulations using Thermo–Calc software (TCFE7: TCS Steel and Fe-alloys Database) were the basis of calculating the solidus and liquidus temperatures of the composites matrix (free-zone regions). Vickers microhardness (load of 0.1 kgf) measurements were made on transverse samples taken from the composites in accordance with EN ISO 6507-1 using an Innovatest Nexus 400. 30 measurements were performed as a function of depth. The first indent was located 100 μm from the top surface of composite, and the distance between each indent was also 100 μm .

3 Results and discussion

3.1 Analysis of phase composition of Fe–Ni–Cr–Al–Mo– TiC_p composites and lattice parameter of matrix by XRD

To investigate the phase constitution of Fe–Ni–Cr–Al–Mo– TiC_p composites, X-ray diffractometry was conducted. The XRD patterns presented in Fig. 4 show strong peaks at 2θ of about 50.99°–51.29°, 59.32°–59.58°, 89.25°–89.74°, 110.68°–111.52°, and 118.72°–119.12°. They were identified as belonging to Fe_γ planes (111), (200), (220), (311), and (222), respectively. The presence of much weaker peaks at 2θ range 41.87°–41.99°, 48.87°–48.93°, 71.57°–71.65°, 86.44°–86.72°, and 91.29°–91.87° corresponds to TiC crystallographic planes. The calculated relative peaks intensities (Table 2) illustrated that the austenite

Fig. 4 The XRD spectra of Fe–Ni–Cr–Al–Mo– TiC_p composites (ICDD 00–033-0397, ICDD 00–006-0614)

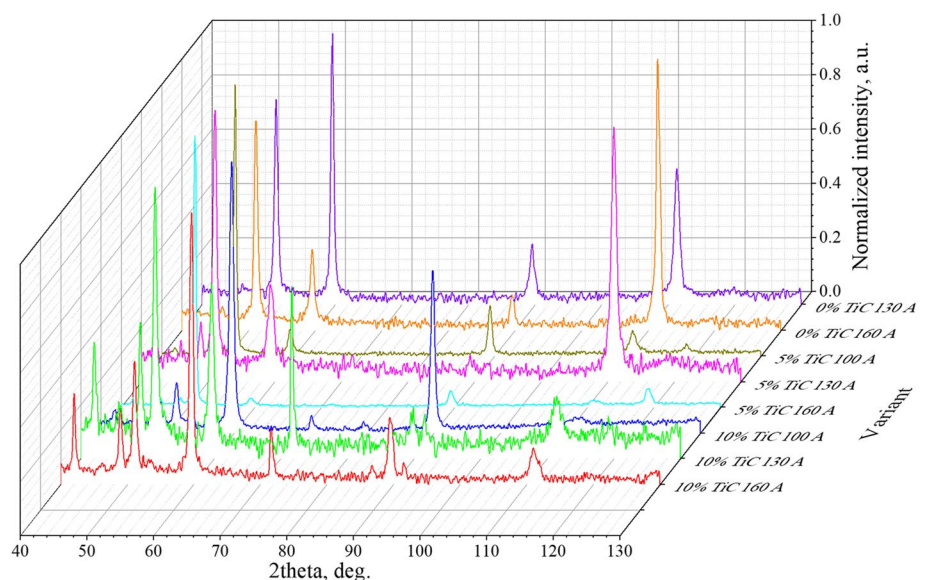


Table 2 Comparison of the peak intensities for Fe_γ

Variant	Concentration of TiC _p (wt%)	Current I (A)	Fe-based austenite		
			$I_{(200)}/I_{(111)}$	$I_{(220)}/I_{(111)}$	$I_{(311)}/I_{(111)}$
1	0	130	1.11	0.38	0.94
2		160	0.42	0.18	1.33
3		100	0.17	0.26	0.18
4	5	130	0.44	0.06	1.26
5		160	0.05	0.11	0.06
6		100	6.40	3.43	0.24
7	10	130	0.85	0.17	0.36
8		160	2.14	0.74	0.62
Standard value acc. to ICDD 00–033-0397			0.45	0.26	0.30

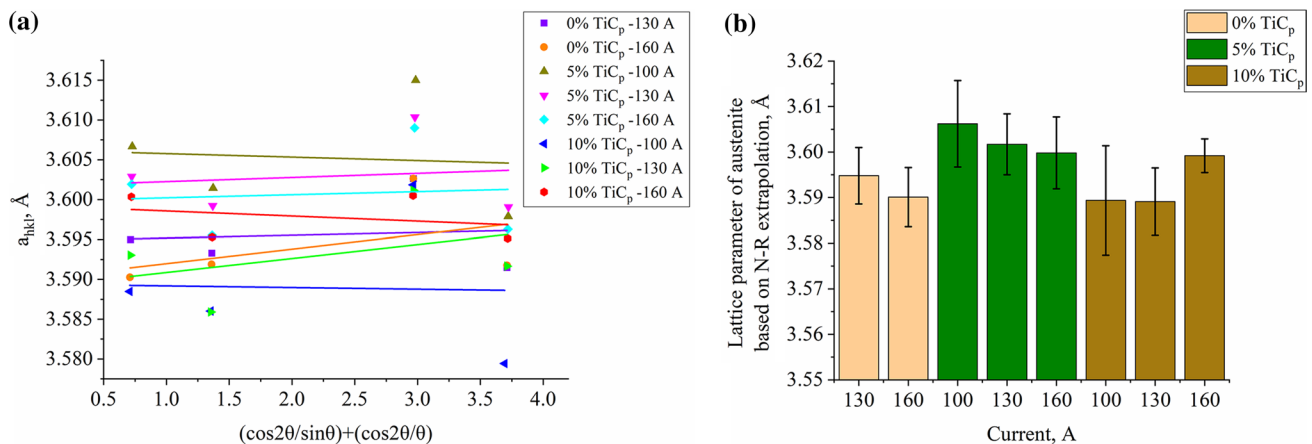
in composites has a texture in variants 5, 6, and 8. They characterized I_{200}/I_{111} ratio strongly varied from the standard, 0.05 (9 times lower), 6.40 (more than 14 times higher), and 2.14 (almost 5 times higher), respectively. The composite no. 6 revealed also a high I_{220}/I_{111} ratio for austenite. Generally, in the case TiC_p, the texture was not observed and particles were randomly distributed. No preferred orientation relationship between particles and matrix was detected. As solidification texture depends on the local heat flow directions and competitive grain growth, no preferred growth directions related to the process condition, like deposition parameters or content of TiC_p, were observed.

For the austenite matrix, the lattice parameter is a little different from the standard data for Fe_γ in AISI304 (3.60 Å), because the Fe (radius-1.56 Å) is strengthened by alloying elements with various atomic radii (Ni-1.49 Å, Cr-1.66 Å, Al-1.18 Å, and Mo-1.9 Å) [32]. For the FCC structure based on Ni: $a = 3.43$ Å (ICDD 01-077-9326). The lattice parameter estimated by N–R was fitted with linear regression (Fig. 5a) and then for each variant presented in Fig. 5b. In the particle-free layers, the lattice parameter was 3.5948 Å (130A) and 3.5901 Å (160 A), respectively. In

the composites with 5% TiC_p addition, it was in the range 3.5998–3.6062 Å, whereas in composites with 10% TiC_p, the calculated lattice parameter of matrix was lower for each deposition current, namely 3.5891–3.5992 Å.

3.2 Microstructural characterization of Fe–Ni–Cr–Al–Mo–TiC_p composites

The microstructures of TiC_p-free layers are shown in Fig. 6a, b. They were characterized by a homogenous structure without unacceptable discontinuities and local porosity did not exceed 0.15%. The introduction of TiC_p into the Ni–20Cr–1.5Al mixtures caused significant microstructural changes. Composites produced at 100 A and 130 A, both with 5% TiC_p, comprised numerous defects like cracks and single pores with the radius even 50 μm (Fig. 6c, d). Increasing the current to 160 A produced an MMC without microcracks and excessive porosity (Fig. 6e). The composite with 10% TiC_p deposited at 100 A was characterized by large porosity and many cracks in close vicinity of the surface. When the current was 160 A, almost all pores were closed (Fig. 6f, h). Deposition of 68.5Ni–20Cr–1.5Al–10TiC_p at

**Fig. 5** **a** Nelson–Riley extrapolation of matrix lattice parameter in Fe–Ni–Cr–Al–Mo–TiC_p composites; **b** Fe-based austenite lattice parameter

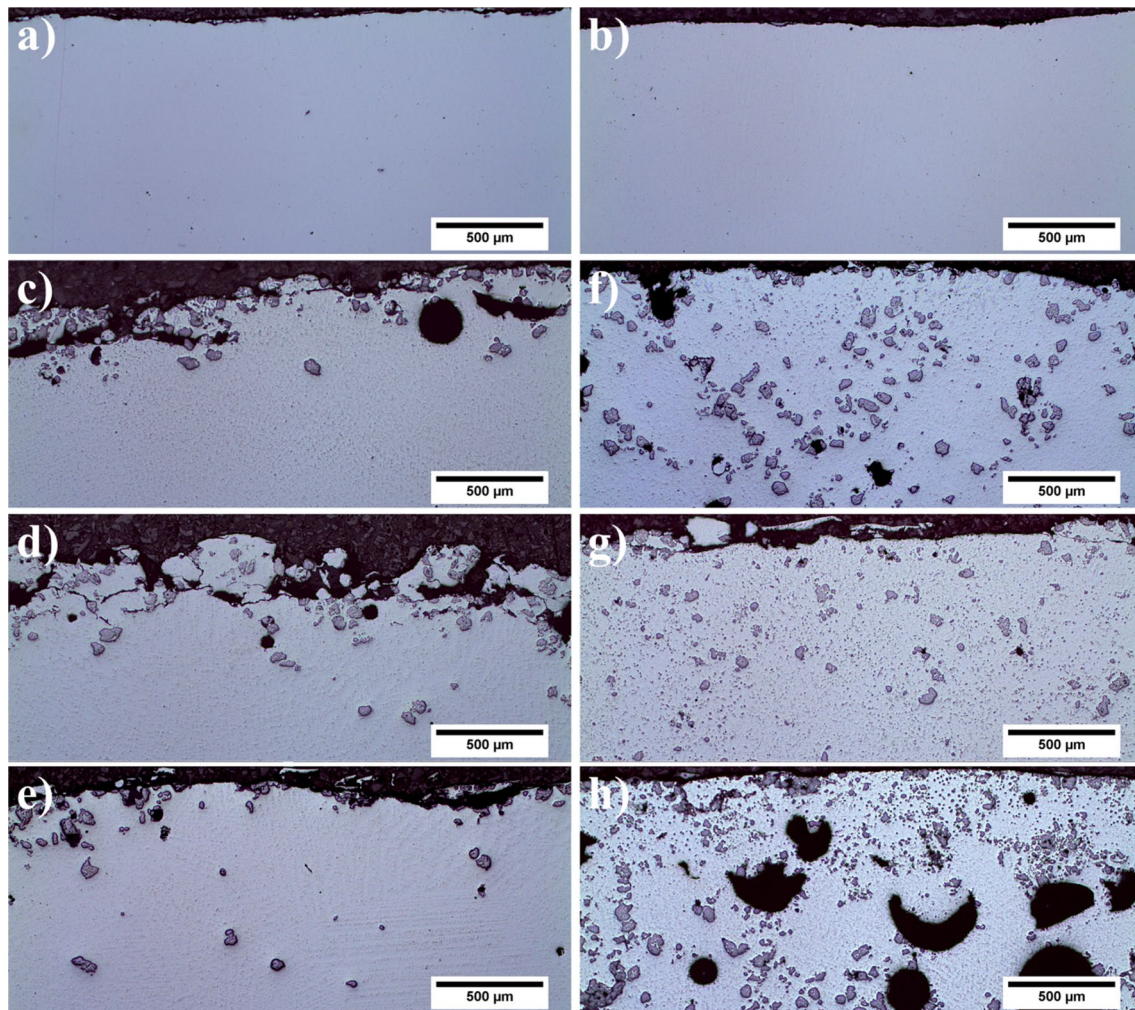


Fig. 6 Microstructure of Fe–Ni–Cr–Al–Mo–TiC_p composites: 0% TiC_p—**a** 130 A; **b** 160 A; 5% TiC_p—**c** 100 A; **d** 130 A; **e** 160 A; 10% TiC_p—**f** 100 A; **g** 130 A; **h** 160 A

130 A ensured definitely the best quality, without large porosity and cracks (Fig. 6g). The presence of defects was caused by the formation of large particle clusters leading to a formation of microstructure where TiC_ps were not covered by the metal matrix. The depth of the large carbides presence was much larger when the initial TiC_p content in the powder mixture was 10%. In the middle region, small precipitates predominated, while large occurred only locally. Arsenault [33] has shown that deformation in cluster zones promotes stress concentration and subsequently early cracks formation. Near the external surface, such regions with large TiC_p contents were present. These can be a significant advantage when the composites will be exposed to abrasive and wear service environment. During the deposition process, the driving forces for fluid flow in the liquid pool are buoyancy force, Lorentz force, shear stress caused by the surface tension gradient at the liquid pool surface (Marangoni convection), and the shear stress having an effect on the liquid

surface by arc plasma [34]. The irregular distribution of the TiC particles can be interpreted by the acting of the first of these, the buoyancy force. The density of the used metal powders (Ni—8.9 g/cm³ and Cr—7.15 g/cm³) is higher than for titanium carbides (TiC—4.93 g/cm³), which induced moving up of large particles [35].

The vicinities of the external edges consisted of large TiC particles, closed porosity, voids filled by liquid metal during deposition, and also brittle cracks (Fig. 7). The source of these cracks was probably thermal stresses originating from different thermal expansion coefficients of the metallic matrix and ceramic particles. The liquid matrix could interact with carbides and generate deformation due to the numerous open spaces. The cross-sections of particles confirmed previous observation of raw powder that took a conglomerate morphology. Between large TiC particles, the smaller were regularly distributed. The reason for the high fraction of small particles could be the disintegration of large

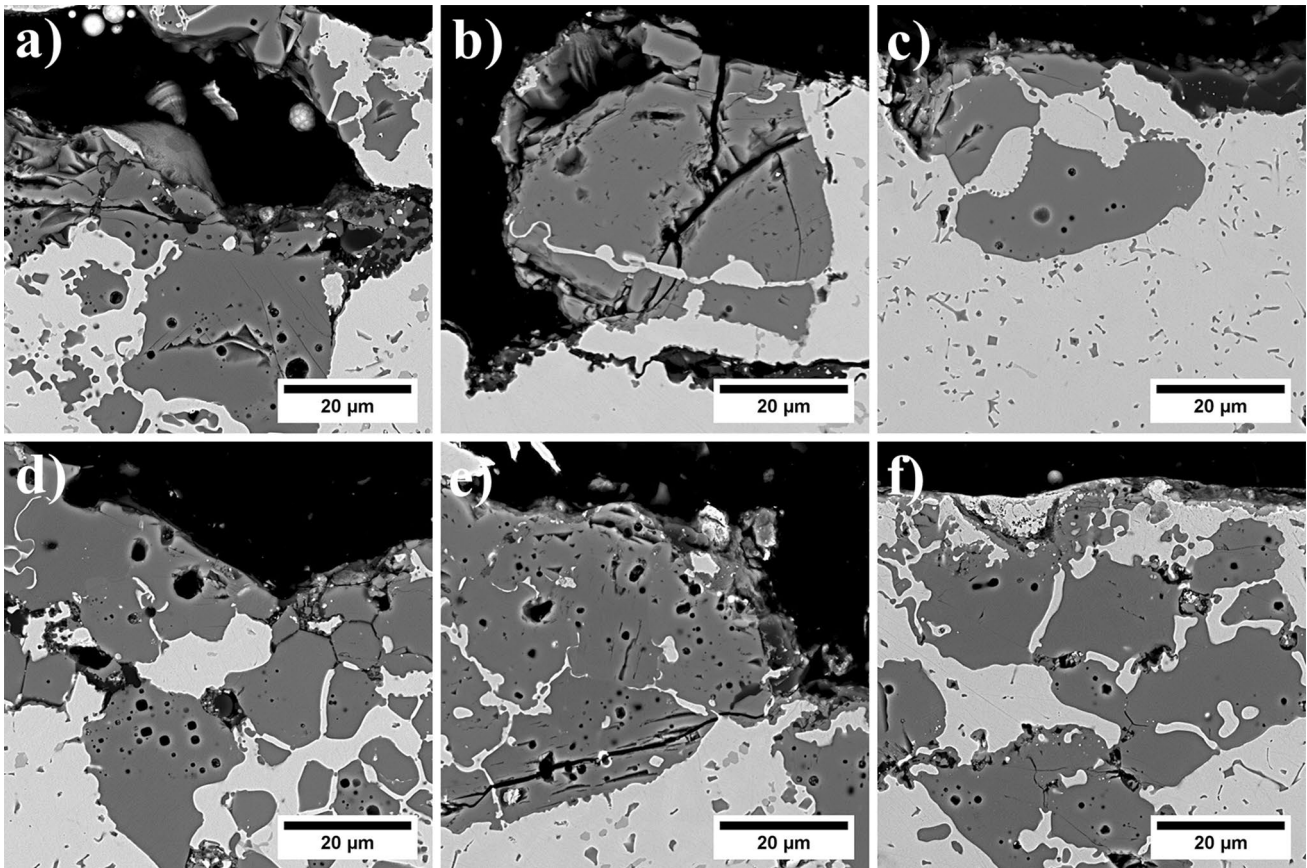


Fig. 7 Near-surface microstructure with large TiC_p particles in Fe–Ni–Cr–Al–Mo– TiC_p composites: 5% TiC_p —**a** 100 A; **b** 130 A; **c** 160 A; 10% TiC_p —**d** 100 A; **e** 130 A; **f** 160 A

particles, probably caused by the mixing of powders and also their subsequent interaction with arc and liquid metal during deposition. Fine particles above and below horizontal line of the plate were subjected to image analysis to calculate their stereological parameters (Figs. 8, 9). The microstructure of composites produced using the 73.5Ni–20Cr–1.5Al–5 TiC_p powder mixtures consisted of a volume fraction of fine TiC_p between 2.7 and 3.5% above the horizontal line of the steel plate, and almost the same 2.7–3.4% below (Fig. 10a). The highest values obtained in the composite fabricated at 100 A were probably due to the poorest mixing of powder with the steel, compared to higher currents. Using 68.5Ni–20Cr–1.5Al–10 TiC_p mixtures, the volume fraction of fine precipitates increased, while more clearly above the horizontal line of the steel plate. The highest values of 5% and 7.9%, depending on the analyzed region, were obtained at 130 A deposition current. The shape factor ζ was calculated to define the TiC_p morphology. Generally, the perfectly spherical precipitates assume a value of 1, and cubic 0.785, whereas in this work for the majority of fine precipitates ζ deviated from these values (Fig. 10b). The shape factor of precipitates in composites produced with 10% TiC_p addition

had only insignificantly lower values than with 5% TiC_p , indicating slightly more complex form of particles in all composite variants. Current of the deposition did not influence strongly the TiC_p morphology. The size of the particles was represented by an equivalent radius, and then, the histogram was subjected to Kernel smoothing (Fig. 11). In each composite, the fine particles with an equivalent radius in the range 0.25–0.6 μm dominated. Only a small fraction of these precipitates above horizontal line of steel plate had an equivalent radius exceeding 1.5 μm .

3.3 Analysis of chemical composition of Fe–Ni–Cr–Al–Mo– TiC_p composites

The composites were subjected to chemical composition analysis by SEM–EDX to reveal the microsegregation of alloying elements. Results are presented separately for each element, Fe, Ni, Cr, Al, Mo, and Ti (Fig. 12). The content of the main element, i.e., iron, whose concentration in layers without TiC_p was 56.6–61.4 at.%. In the composites with the addition of particles, it was 45.2–56.0 at.% (5% TiC_p) and 43.1–55.2 at.% (10% TiC_p). The second element in the

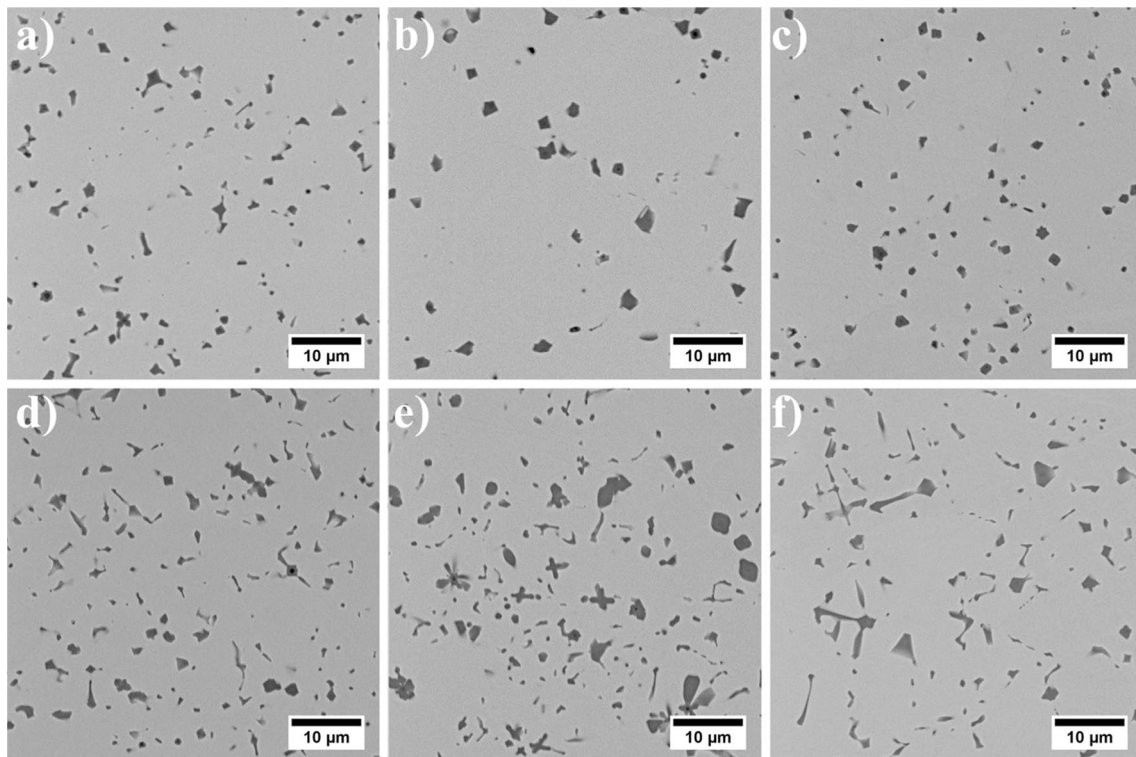


Fig. 8 Microstructure of fine TiC_p particles in Fe–Ni–Cr–Al–Mo– TiC_p composites above the horizontal line of the steel plate: 5% TiC_p —**a** 100 A; **b** 130 A; **c** 160 A; 10% TiC_p —**d** 100 A; **e** 130 A; **f** 160 A

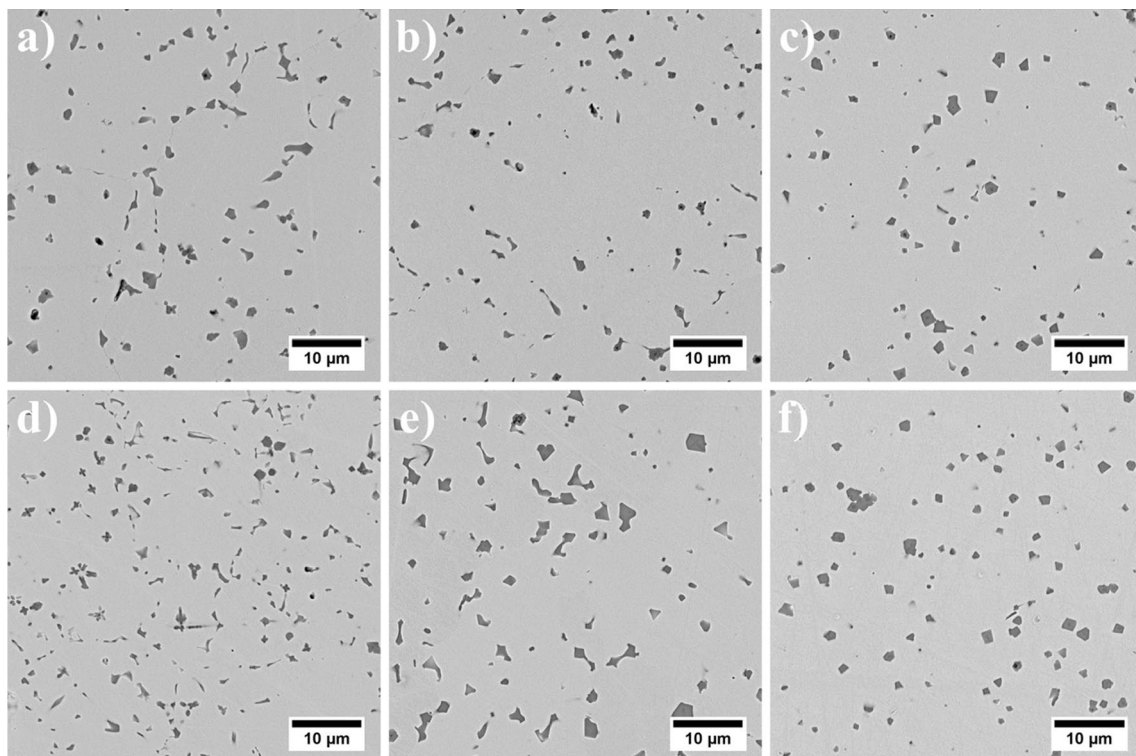


Fig. 9 Microstructure of fine TiC_p particles in Fe–Ni–Cr–Al–Mo– TiC_p composites below the horizontal line of the steel plate: 5% TiC_p —**a** 100 A; **b** 130 A; **c** 160 A; 10% TiC_p —**d** 100 A; **e** 130 A; **f** 160 A

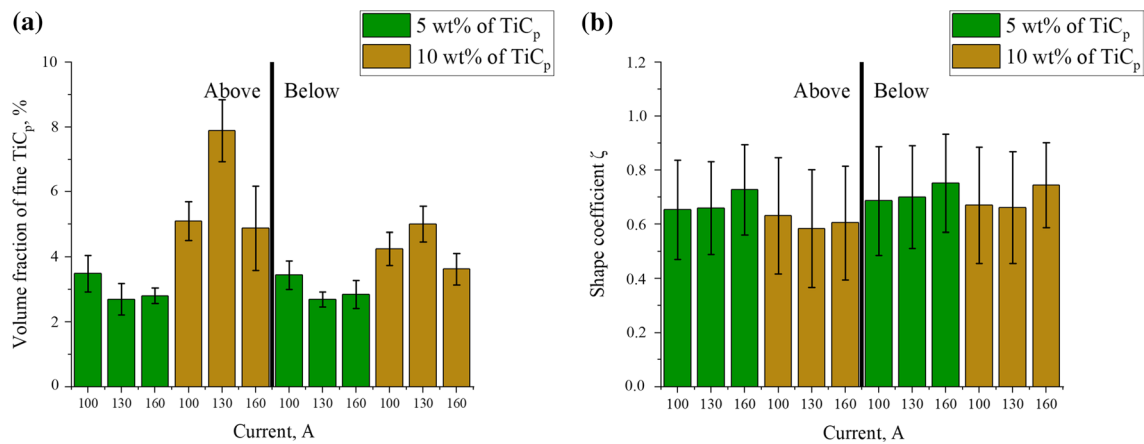


Fig. 10 Stereological parameter of the fine TiC_p particles above and below horizontal line of steel plate: **a** volume fraction; **b** shape coefficient ζ

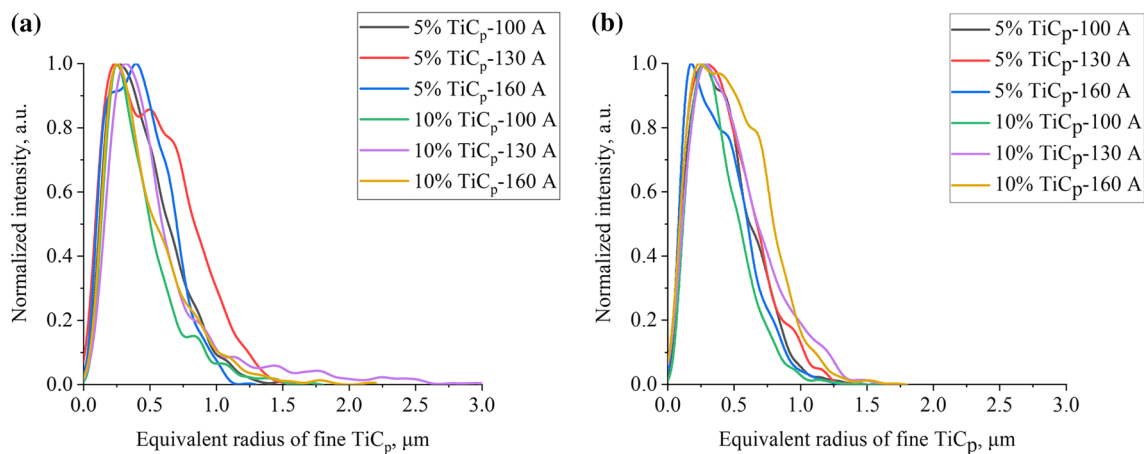


Fig. 11 Equivalent radius of the fine TiC_p particles: **a** above horizontal line of the steel plate; **b** below horizontal line of the steel plate

composition was Ni. Its concentration in particle-free layers was 28.1 at.% for the 130A and 31.9 at.% for 160 A current deposition. In composites with 5% TiC_p , nickel concentration was 25.2–32.6 at.%, while in with 10% TiC_p in a narrower range 27.4–31 at.%. Relatively large differences in Cr concentration were observed between composites with TiC_p addition in comparison with those without particles. The Cr content in layers without TiC_p deposited at 130 A and 160 A was 7.5 at.% and 8.6 at.%, respectively. The chromium concentration range 12.0–18.1 at.% was obtained in composites strengthened by 5% TiC_p , while a slightly wider range of 9.8–16.7 at.% when the initial TiC_p content was 10%. A similar trend as to Cr was noted for Al, because in layers without TiC_p , its concentrations were smaller than in composites with TiC_p addition. Mo concentration, which is an alloying element in 10CrMo9-10 steel, reached slightly higher values in layers without the addition of TiC_p . The addition of 5% TiC_p to the powder mixture resulted in a concentration of Ti in ex-situ composites of 2.5–3.1 at.%,

and when the addition was 10%, the concentration in ex-situ composites increased to 4.3–7.0 at.%. Ti concentration in a given composite coincides with the volume fraction of small particles presented in Fig. 10a. It should be noted that values do not include the contribution of large TiC particles located directly near the external surface where the Ti concentration is dominating.

Lack of fusion is among the major problems during the fabrication of MMCs from powdered metals. The microstructure of the fusion line area revealed the correct metallurgical bonding between low-alloy steel and composite in all fabricated variants and also segregation of particles to the crystalline boundaries (Fig. 13). To reveal the distribution of elements in the area encompassing the support plate and composite, SEM–EDX measurements were carried out at a 134 μm distance. At the beginning of the measuring line, the dominant content of Fe was observed, which originated from the support plate, while, after crossing the fusion line, there was a clear increase in the concentration

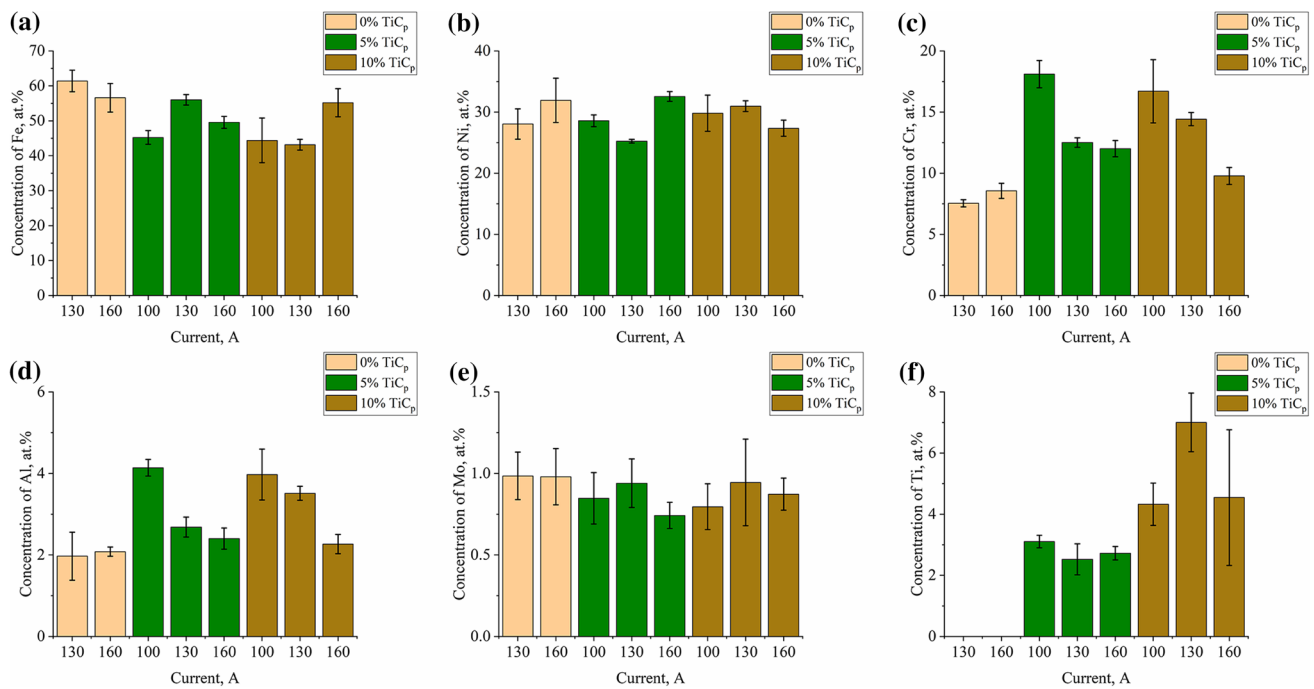


Fig. 12 Distribution of selected alloying element in the Fe–Ni–Cr–Al–Mo–TiC_p composites: **a** Fe; **b** Ni; **c** Cr; **d** Al; **e** Mo; **f** Ti

of elements included in the powder mixture. When there is no TiC_p addition in the layers, the change in Fe concentration on the fusion line occurs in a very short distance. In composites especially with 5% TiC_p, the transition zones were usually smoother, which suggested more intensive mixing during deposition. Despite the difference in the density of alloying elements and particles, TiC_p was present even near the fusion line. Inside the composites, local drops in Fe concentration and simultaneous Ti increase were also revealed, which are associated with the presence of TiC_p. The various Ti concentrations were the result only of the size of the particles through which the measuring line crossed. Some areas enriched in Fe and depleted in Ni have also been locally revealed, which may indicate incomplete mixing of the base material and the melted powder mixture.

3.4 Study of the TiC_p/matrix interface by transmission electron microscopy

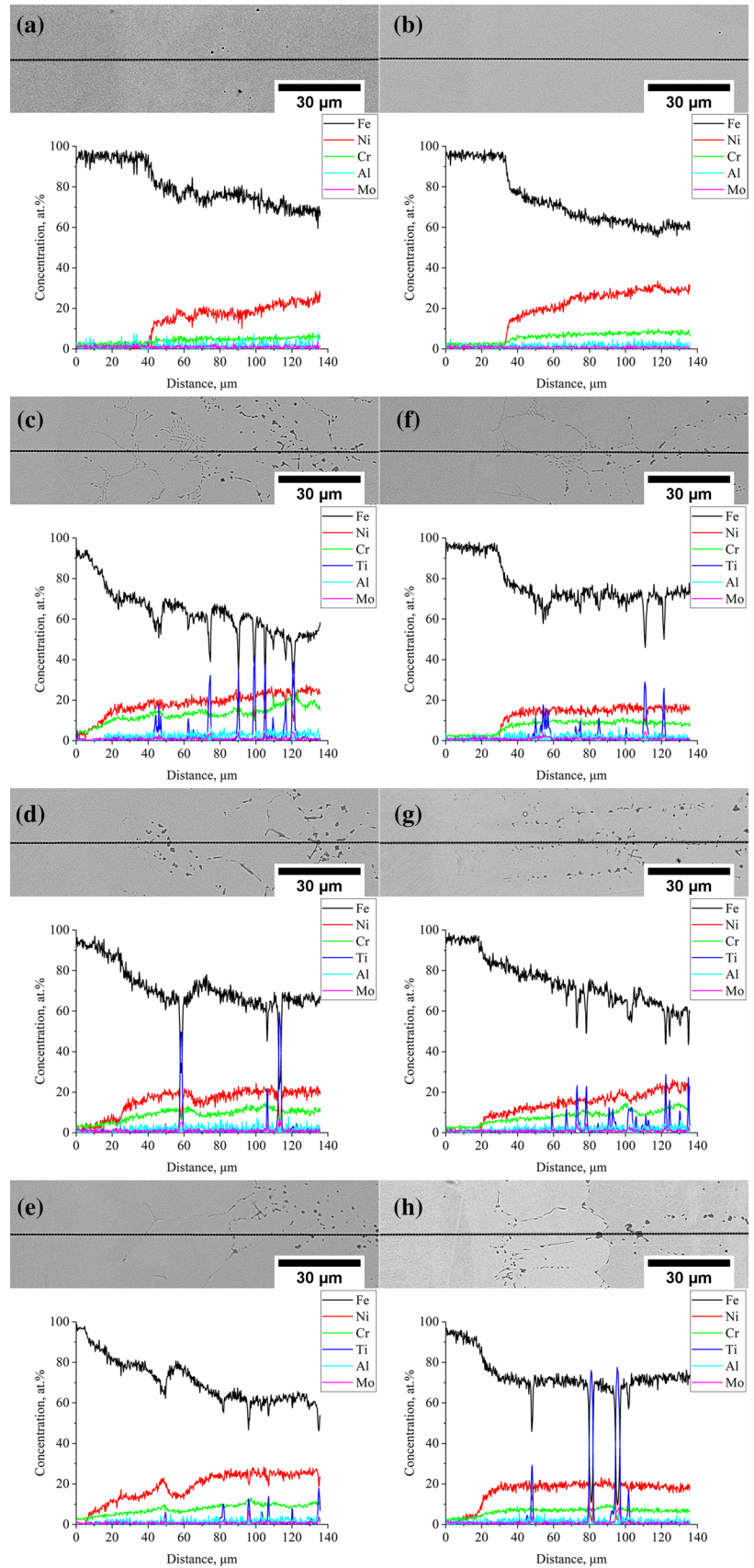
TEM study was mainly focused on determining the interaction between TiC_p and the matrix during the 3DPMD process. Lack of cracks on the interface fine particle/matrix and good metallurgical bonding suggests that they were sufficiently wetted by the liquid matrix (Fig. 14) Mortensen [36] reported that the wetting of particles by liquid metal in MMC solidification processing is affected by both chemical and mechanical effects, the latter embracing fluid flow, heat, and mass transfer phenomena. Selected TEM micrograph of a TiC_p and matrix with corresponding electron diffraction

pattern is shown in Fig. 15. It should be noted that the presented patterns had clear reflections from a face-centered cubic (FCC) crystal structures, but any orientation relationships between MC and γ phases did not exist.

On the edges of TiC_p, only locally, relatively large secondary precipitates with thicknesses of about 40–60 nm and clearly with different contrast were observed (Fig. 16). To obtain more information, the distribution analysis of selected alloying elements in the area showed the matrix, TiC_p, and those secondary phases (Fig. 17). The results suggest that, despite the high stability of TiC at elevated temperatures and limited time for diffusion during deposition, the reaction zone was not limited to only few nanometers. The distribution maps revealed two types of secondary precipitates at the TiC_p edges. The first were enriched in sulfur, which is known to be a harmful element in the γ -matrix alloys, because through the formation of sulfides or carbo-sulfides precipitates can reduce ductility. The second ones were precipitates enriched in chromium, located in the close vicinity of S-rich precipitates.

The accompanying electron diffraction pattern in Fig. 18 demonstrated that the S-rich precipitates were titanium oxide sulfate (TiOSO₄) which possess orthorhombic crystal structure with lattice parameters $a = 10.953 \text{ \AA}$, $b = 5.152 \text{ \AA}$, and $c = 6.426 \text{ \AA}$ [37]. Similarly like titanium carbide, TiOSO₄ precipitates were not coherent with the surrounding matrix. Its presence in the composites was due to the pollution of TiC powder in sulfur and oxygen. The atomic-scale resolution image of Cr-rich phase was

Fig. 13 Distribution of alloying elements across the fusion zone: 0% TiC_p—**a**) 130 A; **b**) 160 A; 5% TiC_p—**c**) 100 A; **d**) 130 A; **e**) 160 A; 10% TiC_p—**f**) 100 A; **g**) 130 A; **h**) 160 A



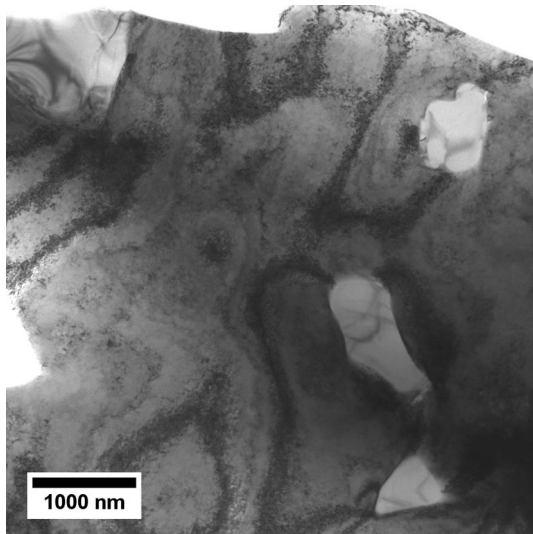


Fig. 14 Microstructure of TiC_p in the matrix by TEM

subjected to FFT which revealed the diffraction pattern (Fig. 19). This pattern clearly showed reflections from $M_{23}C_6$ carbide with Fm-3m cubic crystal structure and lattice parameter $a = 10.65 \text{ \AA}$ [38]. Generally, $M_{23}C_6$ carbides readily form in alloys with moderate and high chromium concentration [39]. In all our composites, Cr content in the γ -matrix exceeded 10 at.%. Their formation was connected with the decomposition of the titanium carbides. In the range 760–980 °C, the most typical transformation described as $MC + \gamma \rightarrow M_{23}C_6 + \gamma'$ can occur [40, 41]. Excess of carbon in the surrounding matrix tends to form $M_{23}C_6$ precipitates that are usually enriched in Cr. In accord with this principal reaction, the intermetallic γ' phase (Ni_3Al) forms, and can coast the $M_{23}C_6$ carbides. The γ' ($L1_2$ structure) usually is characterized by a lattice parameter close to that of the γ -matrix, which can impede their distinguishment on HRTEM images, whereas its diffraction pattern is characterized the additional superlattice reflections [42]. Aluminum is one of the alloying elements in the composites and its slight enrichment near $M_{23}C_6$ occurred, but despite intensive observation, the presence of γ' precipitates was not confirmed. A similar conclusion

Fig. 15 **a** Location of selected area electron diffraction of the γ -matrix and TiC_p ; **b** electron diffraction patterns of the γ (red) and TiC_p (green)

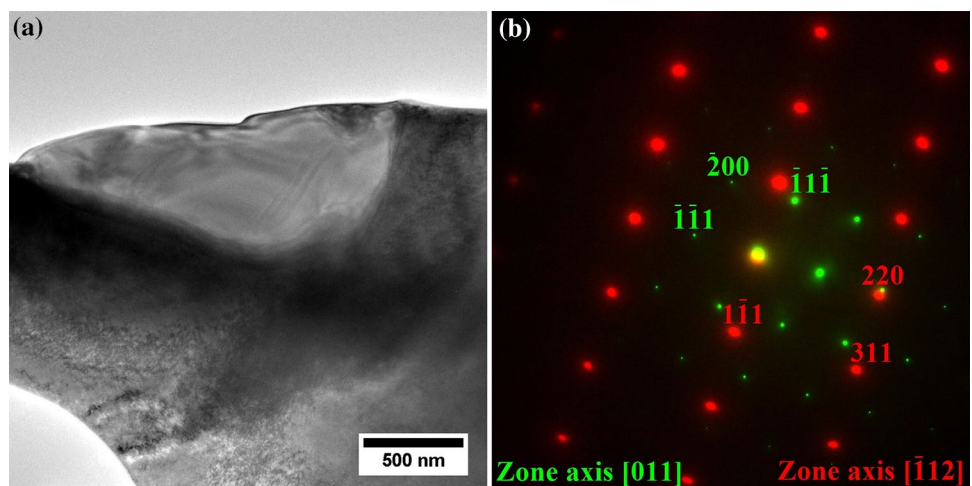
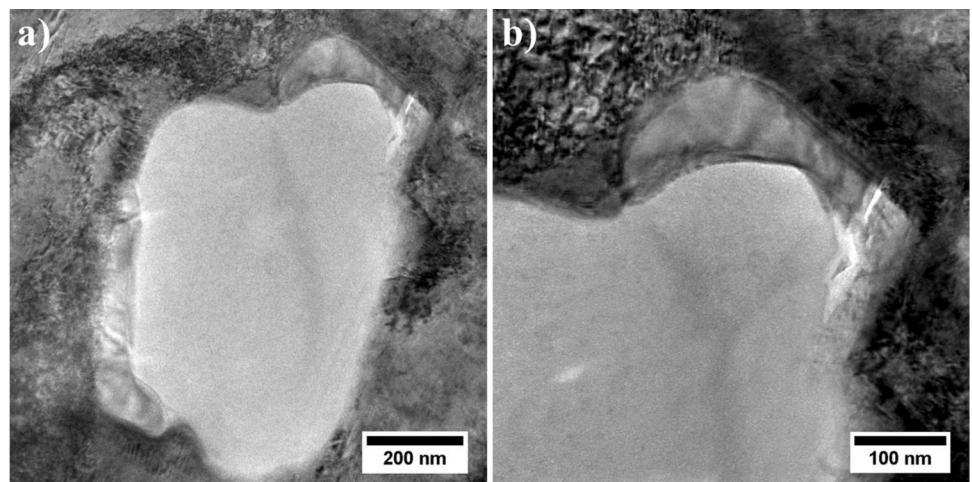


Fig. 16 **a** Microstructure of titanium carbide particle with the secondary phases on the edge; **b** morphology of the nanosize secondary phases



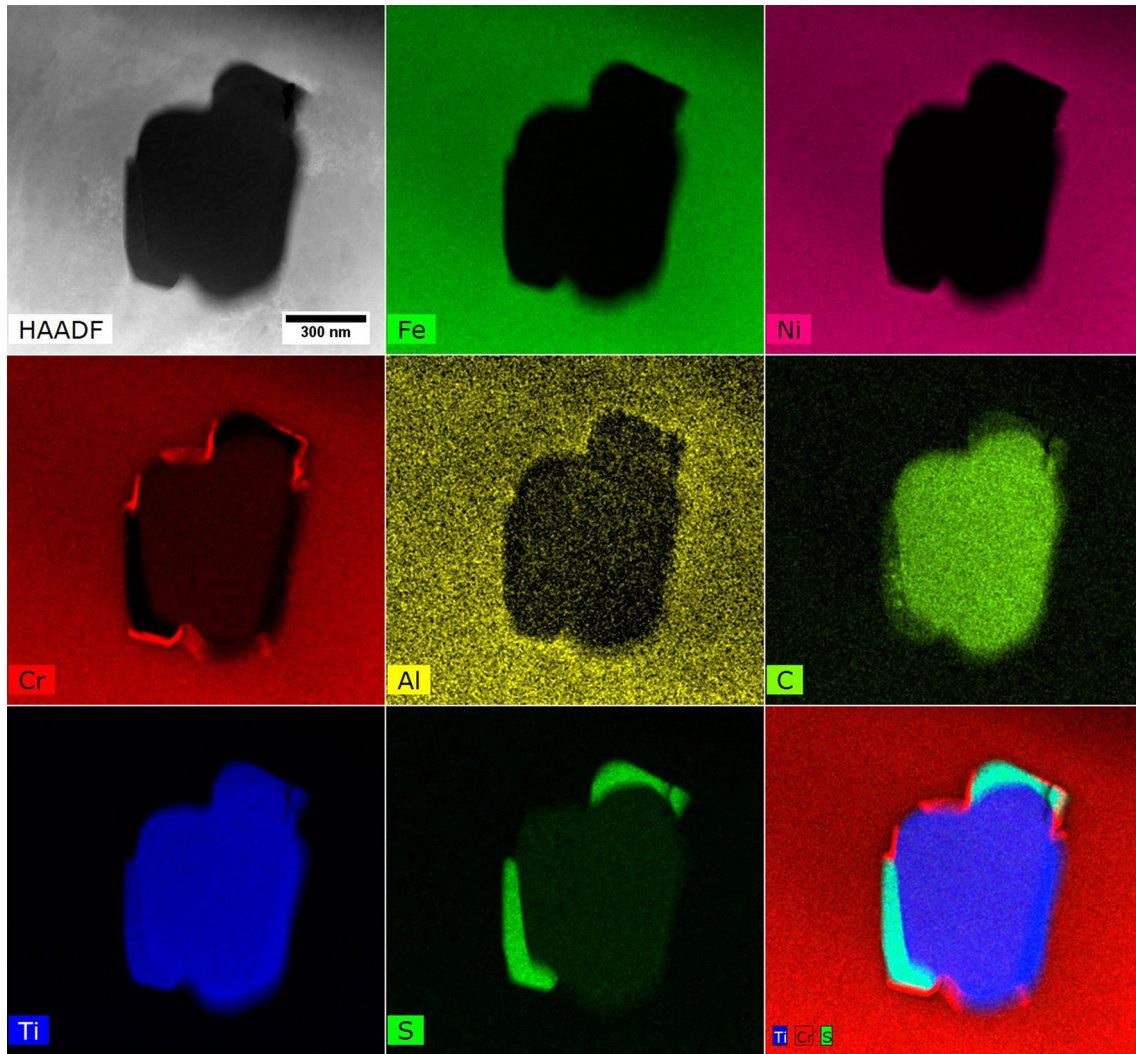


Fig. 17 Distribution of selected alloying elements in the area of matrix, TiC_p , and secondary phases

Fig. 18 **a** Microstructure of titanium carbide particle with the secondary phases on the edges; **b** diffraction pattern of the $TiOSO_4$

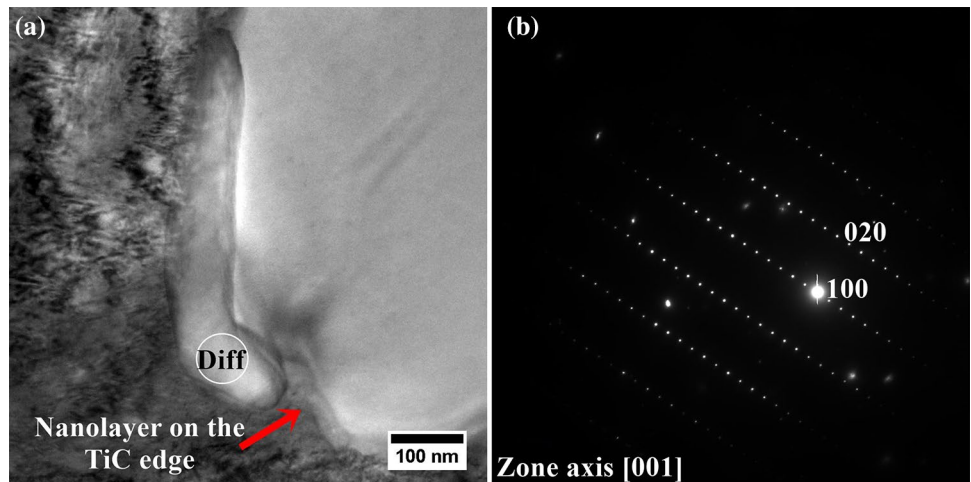
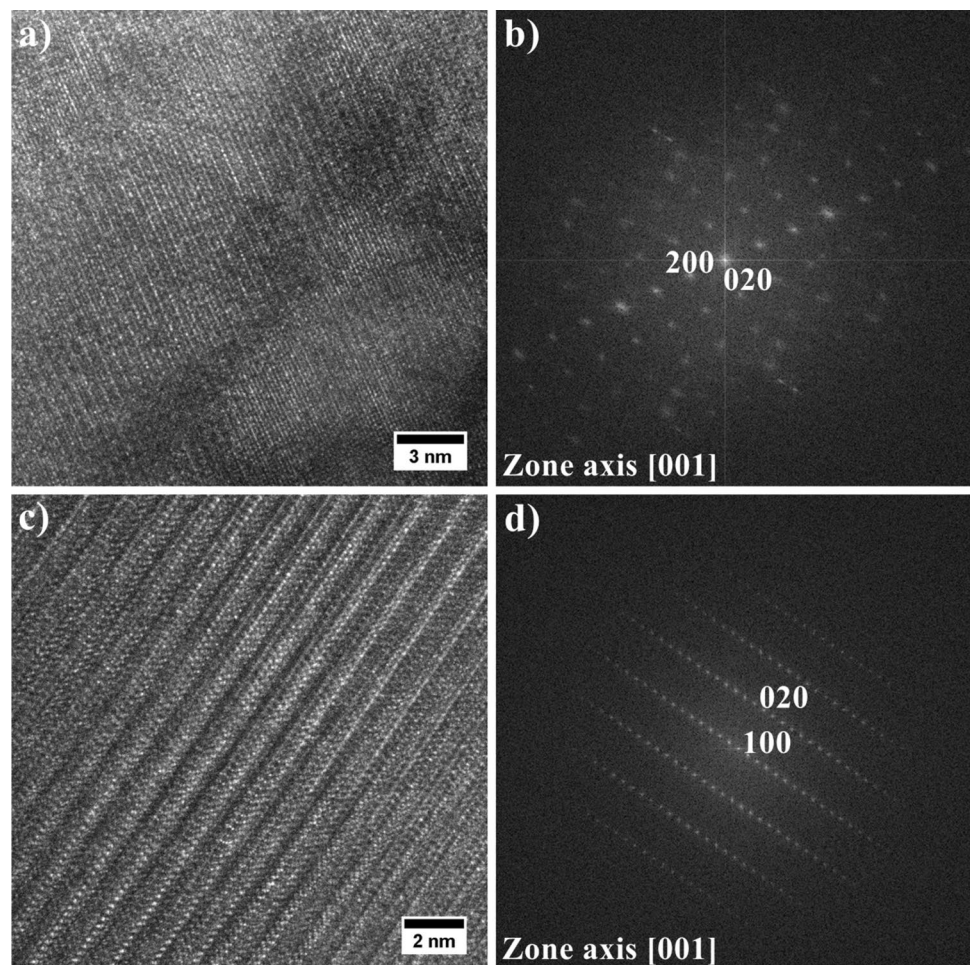


Fig. 19 Secondary phase structure in atomic-scale resolution with corresponding diffraction peaks calculated by fast Fourier transformation (FFT): **a, b** $M_{23}C_6$ and $M_{23}C_6/\gamma$ interface; **c, d** $TiOSO_4$



was formed by Lvov [43] based on the study of primary MC carbide decomposition in the Ni-base superalloys. He observed that the degenerated MC carbides were surrounded by decomposition zones with discrete $M_{23}C_6$ (blocky and lath morphology) precipitates. Using transmission electron microscopy, he confirmed the absence of the γ' phase in the MC decomposition zone in Inconel 738, CC GTD-111 and DS GTD-111. Instead of the γ' , the η - $Ni_3(Ta, Ti)$ was identified. The $L1_2$ crystal structure (γ') is related to that of the DO_{19} (η) and the aluminum addition to Ni-Ti alloys stabilizes the first. During decomposition of (Ta, Ti)C carbides, carbon diffuses more rapidly than titanium and tantalum. Aluminum concentration plays the key role in deciding which phase most favorably forms during MC carbide decomposition. In this study, also the η phase presence was not confirmed. The second way of its formation could be a reaction with the residual carbon in the matrix, but this is excluded, because $M_{23}C_6$ was not detected far away from TiC_p . Based on the information about the crystal structure of detected phases and their chemical composition, the unit cells generated by VESTA software are presented in Fig. 20.

The reactions on the TiC_p /Ni-base alloy interface in laser-synthesized coatings using a mixture 30 vol.% TiC_p and 70% of Ni-16Cr-3.5B-4.5Si-0.8C alloy was also studied by Wu [45]. The high-resolution transmission electron microscopy images of the interface undissolved TiC_p /matrix revealed a thin reaction zone, with an undetermined crystal structure, due to its small size (around 2–5 nm). Based on the TEM-EDX analysis, it was concluded that the layer was a result of reaction of TiC_p with boron. Wu suggested also that interfaces around undissolved TiC particles are thermodynamically unstable and have the kinetic ability to transform into a more stable configuration. Janas [46] in the TEM examination of the interface in Ni_3Al -TiC composite did not observe any secondary precipitates, but only dislocation networks in the matrix. Various phenomena may occur at interfaces, namely epitaxial growth, precipitation, and chemical reactions. In contrast to in-situ MMCs, where reinforcing phases with stable interfaces are directly synthesized in a metallic matrix during composite fabrication, the formation of some intermetallics at the interfaces in ex-situ MMCs can lead to a large weakness of layers.

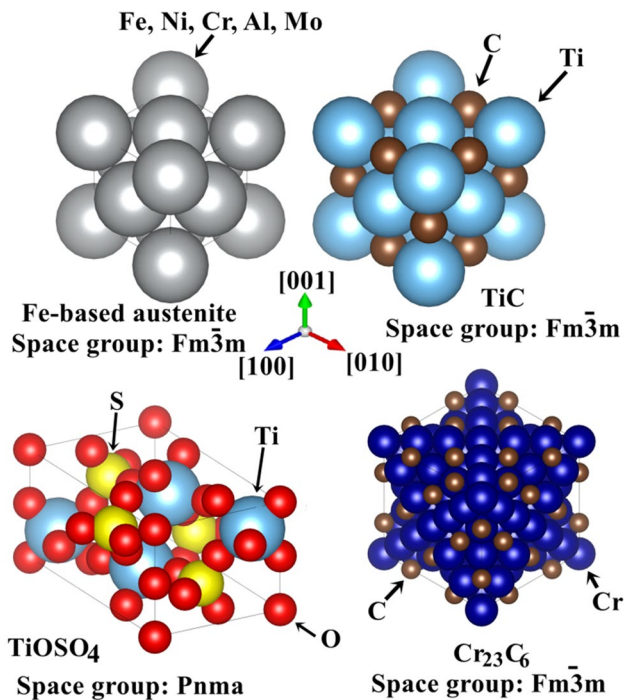


Fig. 20 Unit cell models of phases detected in the composites. Images generated using the VESTA software [44]

3.5 Influence of the chemical composition of matrix on the solidus and liquidus temperatures calculated by ThermoCalc

SEM–EDX analyses revealed an irregular concentration of alloying elements in the matrix. Therefore, measurements in the matrix itself were carried out, and results obtained for each variant are presented in Table 3. Based on the Schaeffler diagram [47] and chemical composition of the composite matrices, it can be concluded that they solidified as primary austenite without delta ferrite. The elements included in the matrix significantly differ in their melting points (Fe—1538 °C, Ni—1455 °C, Cr—1907 °C, Al—660 °C, Mo—2622 °C) [32]. Using SEM–EDX data,

thermodynamic simulations were performed to determine the solidus (T_S) and liquidus (T_L) temperatures. The simulation results confirmed that the matrix surrounding TiC_p was characterized by the FCC structure. The solidus and liquidus temperatures of the matrix in ex-situ composites are presented in Fig. 21. In layers without particles, the solidus was 1437 °C and 1430 °C. For the group of composites nos. 3–5, it was in the range 1419–1439 °C, whereas for the next composites no. 6–8, it was 1418–1436 °C. The liquidus temperature in TiC_p -free layers was 1438 °C and 1446 °C. Composites Fe–Ni–Cr–Al–Mo–5 TiC_p were characterized by liquidus in the range 1427–1447 °C, while the composites Fe–Ni–Cr–Al–Mo–10 TiC_p had almost similar values, 1425–1446 °C. Based on these values, it can be stated that the solidification temperature range of matrix, depending on the composite variant, was 6.8–9.3 °C.

3.6 Influence of the TiC_p addition on the microhardness of Fe–Ni–Cr–Al–Mo– TiC_p composites

Microhardness distribution in the composites is shown in Fig. 22. The particles-free layer produced at 130 A had a hardness $138 (\pm 5) \mu HV0.1$, while for that deposited at 160 A, it was slightly higher, around $146 (\pm 6) \mu HV0.1$. All fabricated composites were characterized by at least 50% higher value, which resulted from the presence of TiC_p . Regardless of the initial content of the TiC_p and deposition parameters, the value did not fall below $200 \mu HV0.1$, usually it was around 250 – $300 \mu HV0.1$. The high values of hardness near the surface resulted from the presence of large particles, especially for the variants with 10% TiC_p addition.

A similar favorable increase of mechanical properties was observed in several MMCs with a Ni-base alloy as the matrix. Jiang [48] observed that, compared with the laser clad Inconel 625 substrate, the hardness and modulus measured by nanoindentation of Inconel 625/nano- TiC_p composite coating were improved by 10.3% and 12.4%, respectively. Saroj [49] investigated the ex-situ composites Inconel 825/ TiC_p fabricated via gas tungsten arc welding in which the

Table 3 The chemical composition of the matrix in Fe–Ni–Cr–Al–Mo– TiC_p composites, at.%

Variant	Composition of powder mixture (wt%)	Current (A)	Fe	Ni	Cr	Al	Mo
1	78.5Ni–20Cr–1.5Al–0 TiC_p	130	61.4 (± 3.1)	28.1 (± 2.5)	7.5 (± 0.3)	2.0 (± 0.6)	1.0 (± 0.1)
2		160	56.6 (± 4.1)	31.9 (± 3.6)	8.6 (± 0.6)	2.1 (± 0.1)	1.0 (± 0.2)
3	73.5Ni–20Cr–1.5Al–5 TiC_p	100	47.8 (± 2.1)	29.5 (± 1.2)	17.7 (± 0.8)	4.2 (± 0.4)	0.7 (± 0.3)
4		130	59.5 (± 1.6)	25.2 (± 1.0)	11.6 (± 0.5)	2.9 (± 0.3)	0.8 (± 0.2)
5		160	52.6 (± 1.4)	33.1 (± 0.8)	10.9 (± 0.5)	2.7 (± 0.3)	0.8 (± 0.3)
6	68.5Ni–20Cr–1.5Al–10 TiC_p	100	47.3 (± 7.0)	31.5 (± 4.0)	16.3 (± 2.4)	4.3 (± 0.7)	0.7 (± 0.1)
7		130	46.8 (± 1.3)	34.0 (± 0.4)	14.9 (± 0.9)	3.7 (± 0.3)	0.6 (± 0.2)
8		160	59.7 (± 3.8)	28.0 (± 2.1)	9.0 (± 1.2)	2.5 (± 0.6)	0.8 (± 0.1)

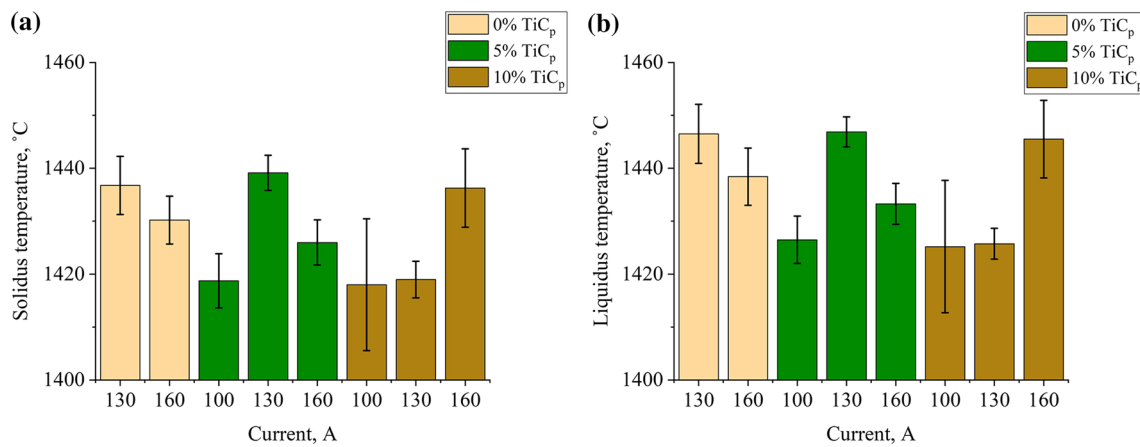


Fig. 21 The equilibrium phase transformation temperatures calculated by ThermoCalc: **a** solidus; **b** liquidus

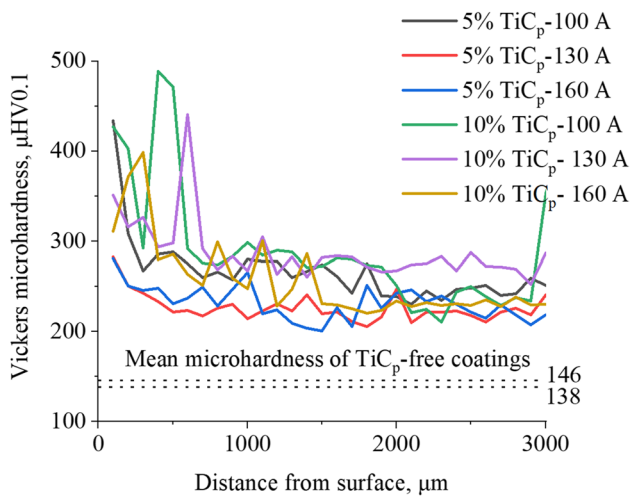


Fig. 22 Microhardness ($\mu\text{HV}0.1$) distribution in Fe–Ni–Cr–Al–Mo–TiC_p composites

content of particles ($\sim 2\text{--}5\ \mu\text{m}$) was 20%, 40%, and 60%. She recorded the microhardness of the fabricated composites $462\ \mu\text{HV}0.05 (\pm 62)$, $680\ \mu\text{HV}0.05 (\pm 160)$, and $770\ \mu\text{HV}0.05 (\pm 225)\ \mu\text{HV}0.05$, respectively, which indicated that, with the increase in TiC_p content, the microhardness of the coatings increases. Wilson [50] researched Inconel 690/TiC_p composites produced by laser deposition and reported that the TiC_p volume of about 40% increased both the hardness (more than two times) and wear resistance. Doğan [51] observed that P/M composites (mainly Fe-based matrix) reinforced by TiC particles were characterized by very good abrasion resistance. Finely distributed fine TiC particles ensured better wear resistance in low-stress abrasion conditions, whereas the coarser TiC particles were more effective in protecting the softer matrix from abrasion in a high-stress environment.

4 Conclusions

- $y\text{Ni-}20\text{Cr-}1.5\text{Al-}x\text{TiC}_p$ ($x=0, 5, 10$; $y=78.5, 73.5, 68.5$) powder mixtures were deposited by 3DPMD on 10CrMo9–10 steel support plates and ex-situ Fe-based austenitic matrix in composites were produced.
- The TiC_p-free layers did not have unacceptable defects, and similar good quality was obtained in two ex-situ composites, namely with 5% TiC_p (160 A current deposition), and with 10% TiC_p (130 A). Large carbide particles were mainly located in close proximity to the outer edge, while fine particles were evenly distributed in the layer volume.
- The volume fraction of fine TiC_p was 2.7–3.5% (73.5Ni–20Cr–1.5Al–5TiC_p mixture) and 4.9–7.9% (68.5Ni–20Cr–1.5Al–10TiC_p mixture) above horizontal line of the steel plate and below 2.7–3.4% and 3.5–5.0%, respectively. The predominating equivalent radius of fine particles was in the range 0.2–0.6 μm in both regions.
- SEM–EDX analyses revealed various chemical compositions of ex-situ composites, resulting from variable initial content of Ni and TiC particles in the powder mixtures, and also strong mixing of the powders with the support steel plate.
- High-temperature exposure during three-dimensional plasma metal deposition process resulted in the reaction of TiC_p with matrix, which can lead to formation of nano-size secondary phases, M_{23}C_6 carbides and TiOSO_4 .
- Thermodynamical simulation results indicated that the highest solidus and liquidus temperatures were obtained for the composite with initial powder mixture 73.5Ni–20Cr–1.5Al–5TiC_p and 130 A current deposition. The lowest phase transformation temperatures were calculated for the composite deposited with the 68.5Ni–20Cr–1.5Al–10TiC_p mixture and 100 A current deposition, respectively, 1418 °C and 1425 °C.

- The hardness of layers without the addition of TiC_p was 138 $\mu\text{HV}0.1$ (130 A) and 146 $\mu\text{HV}0.1$ (160 A), while in the presence of TiC_p , the values did not fall below 200 HV. The higher mean microhardness values were obtained in composites with 10% of TiC_p deposited with 130 A. The hardness was influenced both by the chemical composition of the matrix and contribution of the TiC_p .

Acknowledgements This work was supported by the Polish National Science Centre (Preludium 13) under grant 2017/25/N/ST8/02368. Ł.R. also thanks the DAAD (Research Grants-Short-Term Grants, 2019) for the fellowship at the Chemnitz University of Technology. Authors acknowledge the contribution of KMM-VIN in supporting the collaboration between AGH-UST and Chemnitz University of Technology. The authors wishes to express appreciation to Andrew S. Wronski (University of Bradford) for editing the manuscript.

Compliance with ethical standards

Conflict of interest No potential conflict of interest was reported by the authors.

Open Access This article is licensed under a Creative Commons Attribution 4.0 International License, which permits use, sharing, adaptation, distribution and reproduction in any medium or format, as long as you give appropriate credit to the original author(s) and the source, provide a link to the Creative Commons licence, and indicate if changes were made. The images or other third party material in this article are included in the article's Creative Commons licence, unless indicated otherwise in a credit line to the material. If material is not included in the article's Creative Commons licence and your intended use is not permitted by statutory regulation or exceeds the permitted use, you will need to obtain permission directly from the copyright holder. To view a copy of this licence, visit <http://creativecommons.org/licenses/by/4.0/>.

References

1. Lemos G, Márcio C, Pyczak F, Tetzlaff U. Development of a TiC_p reinforced Ni-based superalloy MMC, with high creep resistance and reduced weight. *Key Eng Mater.* 2017;742:189–96. <https://doi.org/10.4028/www.scientific.net/KEM.742.189>.
2. Sahu P, Banchhor R. Fabrication methods used to prepare Al metal matrix composites—a review. *Int Res J Eng Technol.* 2016;3(10):123–32.
3. Yang X, Li X, Yang Q, Wei H, Fu X, Li W. Effects of WC on microstructure and corrosion resistance of directional structure Ni60 coatings. *Surf Coat Technol.* 2020;385:1–9. <https://doi.org/10.1016/j.surfcoat.2020.125359>.
4. Tomków J, Czupryński A, Fydrych D. The abrasive wear resistance of coatings manufactured on high-strength low-alloy (HSLA) offshore steel in wet welding conditions. *Coatings.* 2020;10(3):219. <https://doi.org/10.3390/coatings10030219>.
5. Shabani A, Toroghinejad M. Study on texture evolution and shear behavior of an Al/Ni/Cu composite. *J Mater Eng Perform.* 2018;27(11):6004–155. <https://doi.org/10.1007/s11665-018-3692-0>.
6. Gu D, Zhang H, Dai D, Xia M, Hong C, Poprawe R. Laser additive manufacturing of nano-TiC reinforced Ni-based nanocomposites with tailored microstructure and performance. *Compos Part B.* 2019;163:585–97. <https://doi.org/10.1016/j.compositesb.2018.12.146>.
7. Hoefler K, Nitsche A, Haelsing A, Mayr P. Manufacturing of titanium components with 3DPMD. *Metals.* 2019;9(5):562. <https://doi.org/10.3390/met9050562>.
8. Rakoczy Ł, Grudzień-Rakoczy M, Cygan R. The influence of shell mold composition on the as-cast macro- and micro-structure of thin-walled IN713C superalloy castings. *J Mater Eng Perform.* 2019;28:3974–85. <https://doi.org/10.1007/s11665-019-04098-9>.
9. Rakoczy Ł, Cygan R. Analysis of temperature distribution in shell mould during thin-wall superalloy casting and its effect on the resultant microstructure. *Arch Civ Mech Eng.* 2018;18:1441–500. <https://doi.org/10.1016/j.acme.2018.05.008>.
10. Epishin A, Link T, Noltze G, Svetlov I, Bokshtein B, Rodin A, Salivan-Neumann R, Oder G. Diffusion processes in multicomponent nickel-base superalloy-nickel system. *Phys Met Metall.* 2014;115:21–9. <https://doi.org/10.1134/S0031918X14010050>.
11. Masoudi M, Hashim M, Kamari H. Characterization of novel Ni–Al₂O₃–SiC nanocomposite coatings synthesized by co-electrodeposition. *Appl Nanosci.* 2014;4:649–56. <https://doi.org/10.1007/s13204-013-0250-9>.
12. Olejnik E, Szymanski Ł, Tokarski T, Opitek B, Kurtyka P. Local composite reinforcements of TiC/FeMn type obtained in situ in steel castings. *Arch Civ Mech Eng.* 2019;19:997–1005. <https://doi.org/10.1016/j.acme.2019.05.004>.
13. Balasubramanian K, Kroupa A, Kirkaldy J. Experimental investigation of the thermodynamics of the Fe-Ti-C austenite and the solubility of titanium carbide. *Metall Trans A.* 1992;23:709–27. <https://doi.org/10.1007/BF02675550>.
14. Rodríguez J, Hoefler K, Haelsing A, Mayr P. Functionally graded SS 316L to Ni-based structures produced by 3D plasma deposition. *Metals.* 2019;9(6):620. <https://doi.org/10.3390/met9060620>.
15. Mortensen A, Cornie J, Flemmings M. Solidification processing of metal-matrix composites. *J Met.* 1988;40:12–9.
16. Grudzień-Rakoczy M, Rakoczy Ł, Cygan R, Kromka F, Pirowski Z, Milkovic O. Fabrication and characterization of the newly developed superalloys based on Inconel 740. *Materials.* 2020;13(10):2362. <https://doi.org/10.3390/ma13102362>.
17. Szala M, Hejwowski T. Cavitation erosion resistance and wear mechanism model of flame-sprayed Al₂O₃–40%TiO₂/NiMoAl cermet coatings. *Coatings.* 2018;8(7):254. <https://doi.org/10.3390/coatings8070254>.
18. Li S, Kondoh K, Imai H, Chen B, Jia L, Umeda J, Fu Y. Strengthening behavior of in situ-synthesized (TiC-TiB)/Ti composites by powder metallurgy and hot extrusion. *Mater Des.* 2016;95:127–32. <https://doi.org/10.1016/j.matdes.2016.01.092>.
19. Singh H, Hayat M, Zhang H, Das T, Cao P. Effect of TiB₂ content on microstructure and properties of in situ Ti–TiB composites. *Int J Miner Metall Mater.* 2019;26(7):915–24. <https://doi.org/10.1007/s12613-019-1797-6>.
20. Arsenault R, Fishman S, Taya M. Deformation and fracture behavior of metal-ceramic matrix composite materials. *Progress Mater Sci.* 1994;38:1–157. [https://doi.org/10.1016/0079-6425\(94\)90002-7](https://doi.org/10.1016/0079-6425(94)90002-7).
21. Feldshtein E, Dyachkova L, Królczyk G. On the evaluation of certain strength characteristics and fracture features of iron-based sintered MMCs with nanooxide additives. *Mater Sci Eng A.* 2019;756:455–63. <https://doi.org/10.1016/j.msea.2019.04.044>.
22. Rutecka A, Kowalewski Z, Pietrzak K, Dietrich L, Makowska K, Woźniak J, Kostecki M, Bochniak W, Olszyna A. Damage development of Al/SiC metal matrix composite under fatigue, creep and monotonic load condition. *Proc Eng.* 2011;10:1420–5. <https://doi.org/10.1016/j.proeng.2011.04.236>.

23. Karabulut Ş, Gökmen U, Çinicic H. Study on the mechanical and drilling properties of AA7039 composites reinforced with $Al_2O_3/B_4C/SiC$ particles. *Compos B Eng*. 2016;93(15):43–55. <https://doi.org/10.1016/j.compositesb.2016.02.054>.
24. Feldshtein E, Kardapolava M, Dyachenko O. On the effectiveness of multi-component laser modifying of Fe-based self-fluxing coating with hard particulates. *Surf Coat Technol*. 2016;307:254–61. <https://doi.org/10.1016/j.surfcoat.2016.08.068>.
25. Asthana R, Mileiko S, Sobczak N. Wettability and interface considerations in advanced heat-resistant Ni-base composites. *Bull Pol Acad Sci Tech Sci*. 2006;54(2):147–66.
26. Kvashnin D, Firestein K, Popov Z, Corthay S, Sorokin P, Golberg D, Shtansky D. Al–BN interaction in a high-strength lightweight Al/BN metal-matrix composite: theoretical modelling and experimental verification. *J Alloys Compd*. 2019;782:875–80. <https://doi.org/10.1016/j.jallcom.2018.12.261>.
27. Zhang B, Bi G, Nai S, Sun C, Wei J. Microhardness and microstructure evolution of TiB_2 reinforced Inconel 625/ TiB_2 composite produced by selective laser melting. *Opt Laser Technol*. 2016;80:186–95. <https://doi.org/10.1016/j.optlastec.2016.01.010>.
28. Durlu N. Titanium carbide based composites for high temperature applications. *J Euro Ceram Soc*. 1998;19(13–14):2415–9. [https://doi.org/10.1016/S0955-2219\(99\)00101-6](https://doi.org/10.1016/S0955-2219(99)00101-6).
29. Storms EK. The refractory carbides. New York: Academic Press; 1967.
30. Mathe B. Surface Brillouin scattering studies of elastic properties of materials at high temperature, Ph.D. thesis. University of Witwatersrand; 2009.
31. Nelson JB, Riley DP. An experimental investigation of extrapolation methods in the derivation of accurate unit-cell dimensions of crystals. *Proc Phys Soc*. 1945;57:160–77. <https://doi.org/10.1088/0959-5309/57/3/302>.
32. Clementi E, Raimondi DL, Reinhardt WP. Atomic screening constants from SCF functions. II. Atoms with 37 to 86 electrons. *J Chem Phys*. 1967;47:1300–7. <https://doi.org/10.1063/1.1712084>.
33. Arsenault R, Feng C, Wang L. Localized deformation of SiAl composites. *Mater Sci Eng A*. 1991;131:55–68.
34. Kou S. *Welding metallurgy*. 2nd ed. New Jersey: Wiley; 2003.
35. Lide DR. *CRC handbook of chemistry and physics*. 85th ed. Boca Raton: CRC Press; 2004.
36. Mortensen A. Interfacial phenomena in the solidification processing of metal matrix composites. *Mater Sci Eng A*. 1991;135(30):1–11. [https://doi.org/10.1016/0921-5093\(91\)90527-T](https://doi.org/10.1016/0921-5093(91)90527-T).
37. Ahmed M, Fjellvag H, Kjekshus A. Syntheses and crystal structure of titanium oxide sulfates. *Acta Chem Scand*. 1996;50:275–83. <https://doi.org/10.3891/acta.chem.scand.49-0457>.
38. Bowman A, Arnold G, Storms E, Nereson N. The crystal structure of $Cr_{23}C_6$. *Acta Cryst*. 1972;B28:3102–3. <https://doi.org/10.1107/S0567740872007526>.
39. Davis JR. *ASM specialty handbook: Heat-resistant materials*. ASM International; 1997. ISBN: 978-0-87170-596-9.
40. Qin X, Guo J, Yuan C, Chen C, Hou J, Ye H. Decomposition of primary MC carbide and its effects on the fracture behaviors of a cast Ni-base superalloy. *Mater Sci Eng A*. 2008;485(1–2):74–9. <https://doi.org/10.1016/j.msea.2007.07.055>.
41. Rakoczy Ł, Grudzień-Rakoczy M, Cygan R. Influence of melt-pouring temperature and composition of primary coating of shell mold on tensile strength and creep resistance of Ni-based superalloy. *J Mater Eng Perform*. 2019;28(7):3826–34. <https://doi.org/10.1007/s11665-018-3853-1>.
42. Rakoczy Ł, Milkovic O, Rutkowski B, Cygan R, Grudzień-Rakoczy M, Kromka F, Zielińska-Lipiec A. Characterization of γ' precipitates in cast Ni-based superalloy and their behaviour at high-homologous temperatures studied by TEM and in situ XRD. *Materials*. 2020;13(10):2397. <https://doi.org/10.3390/ma13102397>.
43. Lvov G, Levit V, Kaufman N. Mechanism of primary MC carbide decomposition in Ni-base superalloys. *Metall Mater Trans*. 2004;35:1669–79. <https://doi.org/10.1007/s11661-004-0076-x>.
44. Momma K, Izumi F. VESTA 3 for three-dimensional visualization of crystal, volumetric and morphology data. *J Appl Crystallogr*. 2011;44:1272–6. <https://doi.org/10.1107/S0021889811038970>.
45. Wu H, Hong Y. Microstructure and mechanical properties at TiC_p /Ni-alloy interfaces in laser-synthesized coatings. *Mater Sci Eng A*. 2001;318:15–211. [https://doi.org/10.1016/S0921-5093\(01\)01394-6](https://doi.org/10.1016/S0921-5093(01)01394-6).
46. Janas A, Kolbus A, Olejnik E. On the character of matrix-reinforcing particle phase boundaries in MeC and MeB (Me = W, Zr, Ti, Nb, Ta) in-situ composites. *Arch Metall Mater*. 2009;54(2):319–27.
47. Schaeffler A. Constitution diagram for stainless steel weld metal. *Metal Prog*. 1949;56(11):680–680B.
48. Jiang D, Hong C, Zhong M, Alkhayat M, Weisheit A, Gasser A, Zhang H, Kelbassa I, Poprawe R. Fabrication of nano- TiC_p reinforced Inconel 625 composite coatings by partial dissolution of micro- TiC_p through laser cladding energy input control. *Surf Coat Technol*. 2014;249:125–31. <https://doi.org/10.1016/j.surfcoat.2014.03.057>.
49. Saroj S, Sahoo CK, Tijo D, Kumar K, Masanta M. Sliding abrasive wear characteristic of TIG clad TiC reinforced Inconel825 composite coating. *Inter J Refract Met Hard Mater*. 2017;69:119–30. <https://doi.org/10.1016/j.ijrmhm.2017.08.005>.
50. Wilson JM, Shin YC. Microstructure and wear properties of laser-deposited functionally graded Inconel 690 reinforced with TiC . *Surf Coat Tech*. 2012;207:517–22. <https://doi.org/10.1016/j.surfcoat.2012.07.058>.
51. Doğan ÖN, Hawk JA, Tylczak JH, Wilson RD, Govier RD. Wear of titanium carbide reinforced metal matrix composites. *Wear*. 1999;225–229:758–69. [https://doi.org/10.1016/S0043-1648\(99\)00030-7](https://doi.org/10.1016/S0043-1648(99)00030-7).

Publisher's Note Springer Nature remains neutral with regard to jurisdictional claims in published maps and institutional affiliations.